Applied Catalysis B: Environmental 343 (2024) 123558

Contents lists available at ScienceDirect

Applied Catalysis B: Environmental

journal homepage: www.elsevier.com/locate/apcatb

d-electron regulation of Ru clusters via conductive $V_4C_3T_x$ MXene and cation vacancy to boost efficient oxygen evolution

Junzhi Li [a], Lili Wang [b,*], Zeyu Yuan [c], Yilin Li [c], Haitong Tang [a], Dongdong Li [c], Mingrui Wang [c], Jiawen Cui [a], Wei Han [c,*], Guangshe Li [a,*], Liping Li [a,*]

[a] State Key Laboratory of Inorganic Synthesis and Preparative Chemistry, College of Chemistry, Jilin University, Changchun 130012, PR China
[b] State Key Laboratory for Superlattices and Microstructures, Institute of Semiconductors, Chinese Academy of Sciences & Center of Materials Science and Optoelectronic Engineering, University of Chinese Academy of Sciences, Beijing 100083, PR China
[c] College of Physics, State Key Laboratory of Inorganic Synthesis and Preparative Chemistry, International Center of Future Science, Jilin University, Changchun 130012, PR China

ARTICLE INFO

Keywords:
$V_4C_3T_x$ MXene
Cation Vacancies
Ruthenium clusters
Oxygen Evolution
D-electron

ABSTRACT

The design of economical and efficient noble-metal-based catalysts is paramount for sustainable energy production. However, modulating the electronic structures of noble metals so that they serve as efficient active sites remains challenging. In this study, we develop a multi-interfacial Ru/NiFe-LDH@$V_4C_3T_x$ composite by modulating its *d*-electronic states using electron donors and cation vacancies. The fabricated Ru/NiFe-LDH@$V_4C_3T_x$ catalyst exhibits a high mass activity of 7741 mA mg_{Ru}^{-1} at an overpotential of 270 mV and a low overpotential of 231 mV at 10 mA cm^{-2}. Our experimental and density functional theory calculation investigations confirm that the synergistic effect of the $V_4C_3T_x$ MXene and cation vacancies on the electronic structure lowers the d-band center of Ru and weakens the adsorption of the *OOH intermediate at the active Ru atom site. Thus, the catalytic performance of Ru/NiFe-LDH@$V_4C_3T_x$ is significantly improved owing to its reduced energy barrier of the rate-determining step (RDS).

1. Introduction

To reduce dependence on traditional fossil fuels, water electrolysis is regarded an attractive and sustainable technology for hydrogen production [1–6]. Notably, the oxygen evolution reaction (OER) is a crucial half-reaction that limits the efficiency of overall water splitting owing to its sluggish four-electron process [7–10]. Currently, noble-metal-based materials (e.g., Ir and Ru) are considered excellent OER catalysts [11–15]. Although several non-precious metal catalysts have been developed to address the high costs and poor durability of noble-metal-based catalysts, their catalytic activities in alkaline electrolytes are not satisfactory. Thus, creating substrates and coordination environments that are suitable and nontrivial for determining the catalytic performance remains a challenge. Dispersing noble metal single-atom or cluster catalysts on supports is regarded as an effective approach for reducing the loading and improving the atomic utilization of noble metals [1,12,15–21].

To date, various materials have been designed as substrates for anchoring noble metal single-atom (SA) and cluster catalysts [18, 22–31]. Among these materials, layered double hydroxides (LDHs) are promising platforms for the dispersion of noble metal atoms as their tunable two-dimensional (2D) structures with high surface areas [25,32, 33]. Specifically, vacancy engineering is employed to stabilize atoms and manipulate their electronic structures [34,35]. However, the poor electronic conductivity, severe agglomeration, and instability of LDHs hinder their catalytic activities. In addition, the noble metals are ineffective as sites for substrate-supported noble-metal-based catalysts. Moreover, the incorporation of noble metals only modulates the local electronic structure of the substrate to form an active center, which impairs the ability of the noble metal [36]. Generally, 4d/5d block noble metals are known to feature abundant *d*-electronic spatial extents [15], and the *d*-electron configuration is known to correlate with the adsorption energies of intermediates in the OER. Therefore, strengthening the manipulation of *d*-electrons around precious metal sites is crucial to improve catalytic performance. Recently, two-dimensional (2D) carbides (MXene) have been used to improve the electrocatalytic performance owing to multivalent transition metal and high conductivity [37–39]. For instance, Li et al. reported a MXene/RuCo

* Corresponding authors.
E-mail addresses: liliwang@semi.ac.cn (L. Wang), whan@jlu.edu.cn (W. Han), guangshe@jlu.edu.cn (G. Li), lipingli@jlu.edu.cn (L. Li).

https://doi.org/10.1016/j.apcatb.2023.123558
Received 6 September 2023; Received in revised form 22 November 2023; Accepted 23 November 2023
Available online 28 November 2023
0926-3373/

nanoparticle heterostructure electrocatalysts [14], and the catalyst with an optimized *d*-band centers showed excellent OER activity (253 mV at 10 mA cm^{-2}). Ru SA catalyst immobilized on $Ti_3C_2T_x$ MXene was demonstrated to have a high OER activity (290 mV at 10 mA cm^{-2}) [40]. With these observations, highly multivalent conductive materials could be coupled each other to construct multi-heterogeneous interfaces that combines with vacancy strategies, which may create opportunities for tuning *d*-electron structures of noble metals and maximize their catalytic activities as well.

In this study, Ru atom clusters were anchored onto conductive NiFe-LDH@$V_4C_3T_x$ MXene substrates (Ru/NiFe-LDH@$V_4C_3T_x$) via a straightforward hydrothermal and etching strategy. Aberration-corrected high-angle annular dark-field scanning transmission electron microscopy (AC-HAADF-STEM) revealed the coexistence of Ru atoms and vacancies. Electron donation from the conductive $V_4C_3T_x$ MXene and cation vacancies triggered electronic reconfiguration and formed more electron-rich Ru atoms, as verified by the X-ray photoelectron spectroscopy (XPS) and X-ray absorption fine structure spectroscopy (XAFS). As a result, the catalyst Ru/NiFe-LDH@$V_4C_3T_x$ demonstrated remarkable OER performance, with a low overpotential of 231 mV at 10 mA cm^{-2} and an ultralow Tafel slope of 51 mV dec^{-1}. According to density functional theory (DFT) calculations, the electron-rich state of Ru atoms downshifted the d-band center, which weakened the adsorption of the *OOH intermediate and reduced the reaction energy barrier, thus enhancing OER activity. This study presents an efficient approach for regulating Ru as an active catalytic species and provides new insights for designing high-performance noble-metal-based catalysts.

2. Experimental section

2.1. Synthesis of the multilayer $V_4C_3T_x$ MXene

The V_4AlC_3 MAX phase was slowly added to the Teflon lining containing 50% HF and then the Teflon lining was transferred into an oil bath at 50 °C with continuous stirring. After 6 days, the waste etching solution was removed by centrifugation. The precipitate was washed with DI water for several times and dried under vacuum at 60 °C.

2.2. Synthesis of the few-layered $V_4C_3T_x$ MXene

The multilayer $V_4C_3T_x$ MXene powder was evenly dispersed in water using ultrasound. After that, 25% TPAOH solution was added to the multilayer $V_4C_3T_x$ MXene dispersion solution with stirring for 12 h. The slurry was obtained by centrifugation at 5000 rpm. Subsequently, 30 mL DI water was introduced and treated by ultrasound for 1 h. Finally, the dark colloid solution with a concentration of 10 mg mL^{-1} was obtained.

2.3. Synthesis of NiFeAl-LDH@$V_4C_3T_x$

Firstly, 2.4 mmol $Ni(NO_3)_2{\cdot}6\ H_2O$, 0.72 mmol $Fe(NO_3)_3{\cdot}9\ H_2O$, 0.08 mmol $Al(NO_3)_3{\cdot}9\ H_2O$ and 2 g urea were dissolved in 80 mL Teflon lining with 25 mL DI water. Then, 15 mL colloid solution of $V_4C_3T_x$ MXene (150 mg) was added to the above solution with stirring for 1 h. The autoclave with Teflon lining was transferred into the oven and heated at 120 °C for 10 h. After reaction, the precipitate is washed with DI water and separated by centrifugation. The hierarchical catalyst, named as NiFeAl-LDH@$V_4C_3T_x$ was obtained by freeze drying. For comparision, the dosages of $V_4C_3T_x$ MXene were changed to 50 and 250 mg. The as prepared samples were denoted as NiFeAl-LDH@$V_4C_3T_x$-50 mg and NiFeAl-LDH@$V_4C_3T_x$-250 mg. Samples NiFeAl-LDH@$V_4C_3T_x$ with different molar ratio of Ni to Fe (Ni: Fe=1:3 and 1:1) was prepared by the same method.

2.4. Synthesis of Ru/NiFe-LDH@$V_4C_3T_x$

An appropriate amount of NaOH is dissolved in water as solution A (4 M). 5 mg $RuCl_3{\cdot}xH_2O$ was added into 5 mL water as solution B. 100 mg NiFeAl-LDH@$V_4C_3T_x$ powder was added to the solution A with stirring to form dark homogeneous solution. After that, the solution B was slowly dripped and stirred for 12 h. For comparision, samples with different dosages of $RuCl_3{\cdot}xH_2O$ (3 mg and 7 mg) were also prepared as Ru/NiFe-LDH@$V_4C_3T_x$-3 and Ru/NiFe-LDH@$V_4C_3T_x$-7. In addition, Ru/NiFe-LDH was prepared according to the similar process without $V_4C_3T_x$ MXene and Ru/NiFeAl-LDH@$V_4C_3T_x$ was synthesized without etching.

2.5. DFT calculations

VASP with projector augmented method wave (PAW) was performed for calculations using generalized gradient approximation functional (GGA) of Perdew-Burke-Ernzerbof (PBE). A cutoff energy of 500 eV and 3 × 3 × 1 Monkhorst–Pack mesh were applied for calculations of adsorption energy. All models were superlattices that was designed with base vector lengths exceeding 10 Å to prevent interference caused by the periodicity of the lattice (12.0956 Å × 12.0956 Å×36.5173 Å). The vacuum layer of 20 Å is set to avert interactions. The convergence of energy and force were 1.0×10^{-6} eV/atom and 0.01 eV/Å for optimization. The (001) and (002) surfaces of NiFe-LDH and $V_4C_3T_x$ are selected for construct of the model according to TEM and the previous reports. The free energy was calculated by $\Delta G = \Delta E + \Delta ZPE - T\Delta S$ in alkaline media (pH = 14).

3. Results and discussion

3.1. Synthesis and structure analysis of Ru/NiFe-LDH@$V_4C_3T_x$

The synthetic process of Ru/NiFe-LDH@$V_4C_3T_x$ is illustrated in Fig. 1a. First, the few-layered $V_4C_3T_x$ MXene was obtained from V_4AlC_3 by etching and exfoliation (Fig. S1). Then NiFeAl-LDH@$V_4C_3T_x$ was constructed by hydrothermal process. After removing the Al by NaOH, the vacancies were produced and anchoring of Ru atoms were achieved in NiFeAl-LDH@$V_4C_3T_x$ (denoted as Ru/NiFe-LDH@$V_4C_3T_x$).

The morphology of as-synthesized samples and Ru clusters were determined by the Scanning electron microscopy (SEM), transmission electron microscopy (TEM), AC-HAADF-STEM and inductively coupled plasma (ICP). Removing Al from brick-like V_4AlC_3 MAX phase (Fig. S2) produces multilayered $V_4C_3T_x$ MXene with accordion-like structures (Fig. S3). After intercalation and ultrasonic treatment, a sheet-like morphology of few-layered $V_4C_3T_x$ MXene is observed in SEM and TEM images (Fig. S4). The SEM images of NiFeAl-LDH@$V_4C_3T_x$ in Fig. S5a, b confirms that the NiFeAl-LDH nanosheets are distributed homogeneously on the few-layered $V_4C_3T_x$ MXene sheets. The microstructure of NiFeAl-LDH@$V_4C_3T_x$ with different content of $V_4C_3T_x$ (50 $V_4C_3T_x$ and 250 $V_4C_3T_x$) is also shown in Fig. S6, where the NiFeAl-LDH@$V_4C_3T_x$ with a low content of $V_4C_3T_x$ presents uneven distribution. Samples NiFeAl-LDH@$V_4C_3T_x$ with different molar ratio of Ni to Fe (Ni: Fe=1:3 and 1:1) has been prepared by the same method. As shown in Fig. S7, both of them consist of agglomerated nanosheets. Such agglomerated nanosheets hinder the mass diffusion. Notably, Ru/NiFe-LDH@$V_4C_3T_x$ with different content of Ru (Fig. 1b, Fig. S5c and Fig. S8) has the same morphology as NiFeAl-LDH@$V_4C_3T_x$. In other words, the etching and incorporation of Ru atoms do not cause structural collapse. Similarly, the TEM images of NiFeAl-LDH@$V_4C_3T_x$ and Ru/NiFe-LDH@$V_4C_3T_x$ (Fig. S9a, b and Fig. 1c, d) reveal the same distribution of LDH and $V_4C_3T_x$. The Ru atom clusters are clearly visualized by AC-HAADF-STEM at atomic level (Fig. 1e). The bright dots (in olive squares) are attributed to Ru atoms, while the orange ellipses correspond to the vacancies. Besides, the distinction between Ru and transition metal (TM) is further confirmed by linear scanning (Fig. 1f). No obvious Ru nanoparticles are observed. The EDS mapping images of NiFeAl-LDH@$V_4C_3T_x$ and Ru/NiFe-LDH@$V_4C_3T_x$ demonstrate the uniform distribution of Ni, Fe, O, V, Al and Ru elements (Fig. S9c and Fig. 1g). For comparison, the NiFe-LDH, NiFeAl-LDH, Ru/NiFe-LDH,

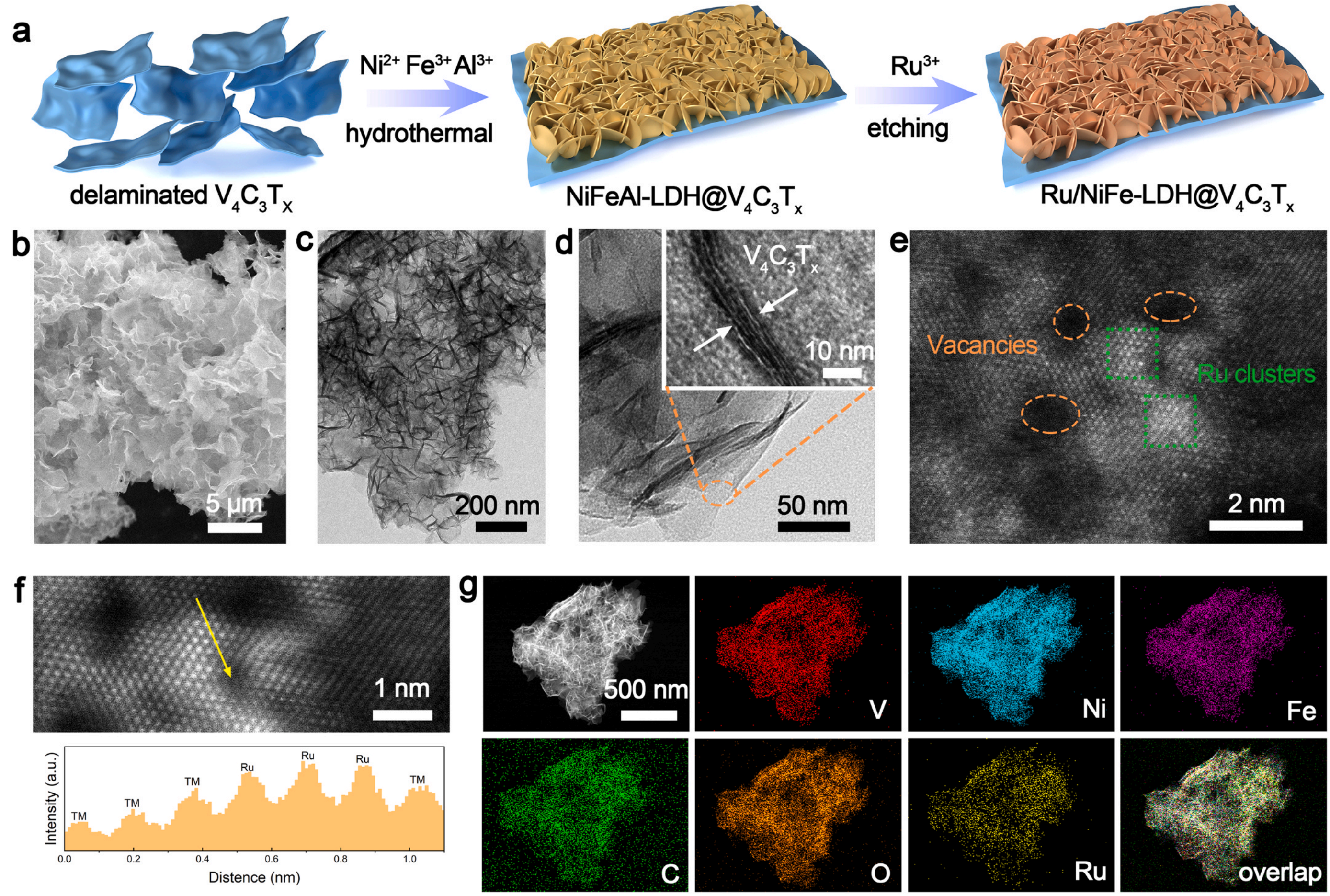

Fig. 1. Morphology characterizations of Ru/NiFe-LDH@$V_4C_3T_x$. (a) Schematic illustration of the synthetic process of Ru/NiFe-LDH@$V_4C_3T_x$. (b) SEM image of Ru/NiFe-LDH@$V_4C_3T_x$. (c, d) TEM images of Ru/NiFe-LDH@$V_4C_3T_x$. Insect of (d) shows HRTEM image of $V_4C_3T_x$ MXene. (e, f) AC-HAADF-STEM images. Vacancies and Ru clusters are identified in oval and square region. (g) EDS mapping images of Ru/NiFe-LDH@$V_4C_3T_x$.

NiFe-LDH@$V_4C_3T_x$ and Ru/NiFeAl-LDH@$V_4C_3T_x$ were also synthesized. The SEM and TEM images illustrate a stacked morphology of NiFe-LDH, NiFeAl-LDH and Ru/NiFe-LDH (Fig. S10a, b and Fig. S11), and the LDH nanosheets are also evenly assembled on $V_4C_3T_x$ MXene for both of the NiFe-LDH@$V_4C_3T_x$ and Ru/NiFeAl-LDH@$V_4C_3T_x$ (Fig. S12 and Fig. S13). The Ru content of Ru/NiFe-LDH, Ru/NiFeAl-LDH@$V_4C_3T_x$ and Ru/NiFe-LDH@$V_4C_3T_x$ determined by ICP are 2.02, 1.75, and 2.04 wt%, respectively (Table S1). The relatively low Ru loading of Ru/NiFeAl-LDH@$V_4C_3T_x$ is mainly due to the absence of an etching process. Etching process produces more vacancies that can help stabilize and load Ru.

The phase components of samples were examined by X-ray diffraction (XRD). The shift of (002) peak from 8.01° to 5.01° and increased intensity (Fig. S14a, b) indicate a complete transformation from the bulk V_4AlC_3 MAX phase to $V_4C_3T_x$ MXene and expanded interlayer spacing. No peaks appeared at $2\theta = 39.88°$ and 43.09° for $V_4C_3T_x$ Mxene confirm the successful etching of Al element. For the samples decorated with LDHs, the typical diffraction peaks of LDHs are observed (Fig. S14c, d). Electron paramagnetic resonance (EPR) has been widely used to detect the unpaired electrons and evaluate ion vacancies [41]. The enhanced EPR signal of NiFe-LDH@$V_4C_3T_x$, comparing with that of NiFeAl-LDH@$V_4C_3T_x$ (Fig. S15), evidence that vacancies are created during the etching process. Besides, the interposition of Ru induces electron rearrangement due to the interaction and electron transfer between Ru and NiFeAl-LDH@$V_4C_3T_x$, NiFe-LDH@$V_4C_3T_x$, which results in the formation of unpaired electrons in the nearby oxygen vacancies or cation defects, thereby giving an enhanced EPR signal of Ru/NiFeAl-LDH@$V_4C_3T_x$ and Ru/NiFe-LDH@$V_4C_3T_x$. To investigate chemical composition, the XPS and X-ray absorption near-edge spectroscopy (XANES) were performed. Ni 2p spectra of all samples (Fig. S16) are deconvoluted into three pair peaks that are assigned to $2p_{3/2}$ and $2p_{1/2}$ and their shake up satellite [42,43]. The Ni 2p peaks of NiFeAl-LDH@$V_4C_3T_x$ show slightly negative shift compared with that of NiFeAl-LDH. After interposition of Ru, the Ni 2p peaks of Ru/NiFeAl-LDH@$V_4C_3T_x$ and Ru/NiFe-LDH@$V_4C_3T_x$ further shift to lower binding energy, while the binding energies of Ni 2p for Ru/NiFeAl-LDH@$V_4C_3T_x$ and Ru/NiFe-LDH@$V_4C_3T_x$ are higher than that for Ru/NiFe-LDH. Such chemical shifts indicate the charge transfer between Ru, NiFe-LDH and $V_4C_3T_x$. For the Fe 2p spectra (Fig. S17), the characteristic peaks of Fe $2p_{3/2}$ are ascribed to Fe^{3+} [7,44,45]. NiFeAl-LDH@$V_4C_3T_x$ and Ru/NiFe-LDH@$V_4C_3T_x$ show an increased binding energy compared with NiFeAl-LDH. In addition, the binding energy of Fe 2p of Ru/NiFe-LDH@$V_4C_3T_x$ is higher than that of Ru/NiFeAl-LDH@$V_4C_3T_x$, indicating the role of vacancies for the electron redistribution. To further understand the charge transfer among components, the V 2p spectra were investigated (Fig. 2a). The peaks at 512.9, 513.9, 515.4 and 516.8 eV in Ru/NiFe-LDH@$V_4C_3T_x$ are assigned to V $2p_{3/2}$ of V-C, V-T_x, V^{3+} and V^{4+}, respectively [46,47]. Notably, the intensity ratio of V^{4+} to V^{3+} increases significantly only in the presence of both Ru and vacancies, indicating that Ru and vacancies can induce the electron donated from $V_4C_3T_x$. Ru $3p_{3/2}$ peak of Ru/NiFe-LDH@$V_4C_3T_x$ (Fig. S18) situates at 462.7 eV is between Ru (0) and Ru (+x) [48,49]. Moreover, the Ru $3p_{3/2}$ peak of Ru/NiFe-LDH@$V_4C_3T_x$ shifts to lower binding energy compared with that of

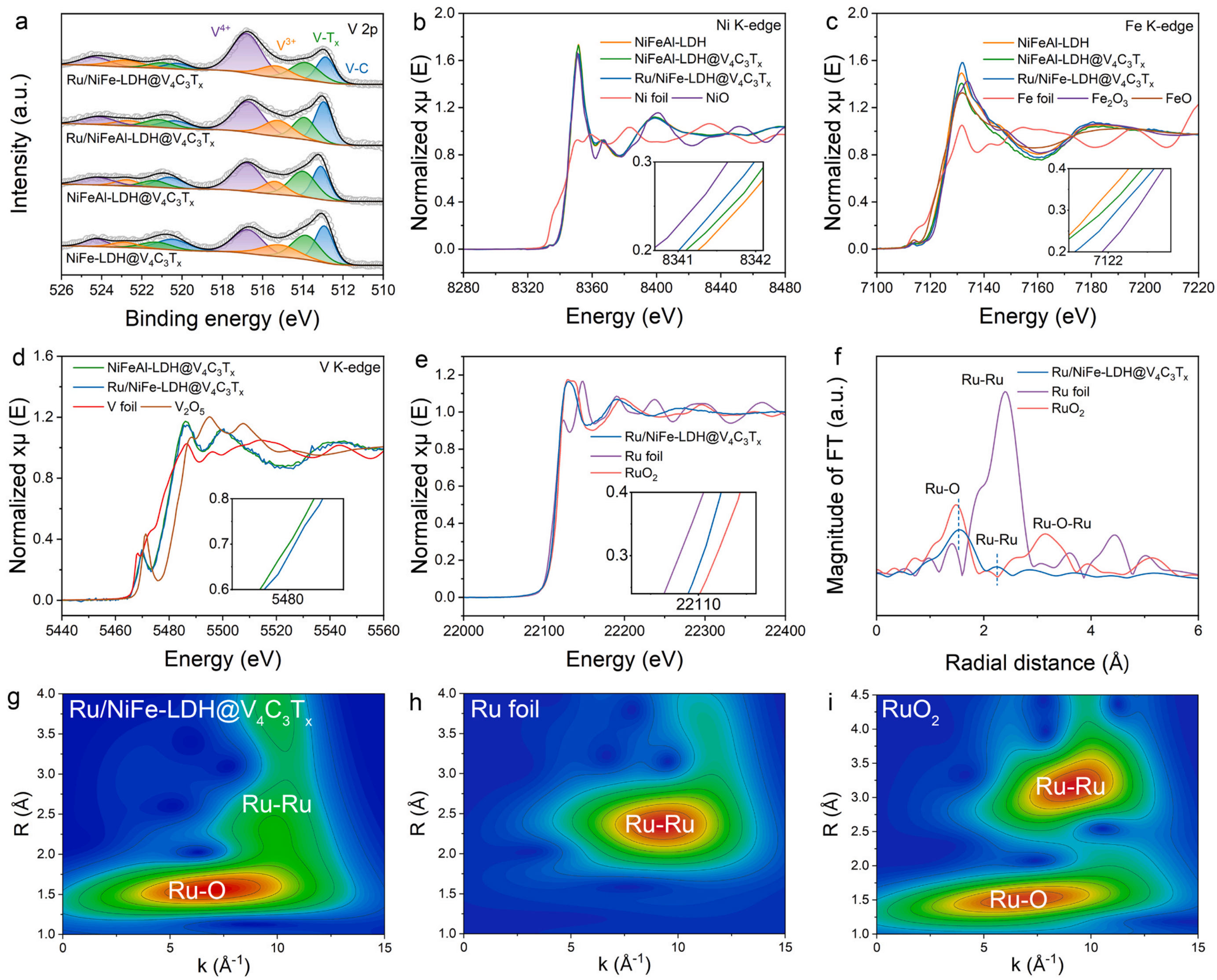

Fig. 2. Electronic state and structure characterization of $Ru/NiFe-LDH@V_4C_3T_x$. (a) V 2p spectra. (b) Ni K-edge XANES. (c) Fe K-edge XANES. (d) V K-edge XANES. (e) Ru K-edge XANES. (f) Fourier-transform (FT) EXAFS spectra of samples at Ru K-edge. (g-i) Wavelet transforms of the EXAFS signals for $Ru/NiFe-LDH@V_4C_3T_x$, Ru foil and RuO_2.

$Ru/NiFeAl-LDH@V_4C_3T_x$ and Ru/NiFe-LDH, exhibiting a rich electron state of Ru in $Ru/NiFe-LDH@V_4C_3T_x$.

Fig. 2b shows the Ni K-edge XANES spectra. The absorption edge positions of NiFeAl-LDH, $NiFeAl-LDH@V_4C_3T_x$ and $Ru/NiFe-LDH@V_4C_3T_x$ shift to higher energy comparing with that of NiO, indicating the coexistence of Ni^{2+} and Ni^{3+} species [43]. Meanwhile, the Ni K-edge position of $NiFeAl-LDH@V_4C_3T_x$ and $Ru/NiFe-LDH@V_4C_3T_x$ lower than that of NiFeAl-LDH, which is consistent with XPS. The nearly close Fe K-edge of as-prepared NiFeAl-LDH, $NiFeAl-LDH@V_4C_3T_x$ and $Ru/NiFe-LDH@V_4C_3T_x$ to the standard Fe_2O_3 (Fig. 2c) reveals their presence of Fe^{3+} species [35]. Different from Ni K-edge, the Fe K-edge absorption edges of $NiFeAl-LDH@V_4C_3T_x$ and $Ru/NiFe-LDH@V_4C_3T_x$ exhibit a shift to higher energy compared with NiFeAl-LDH. In addition, the V K-edge of $Ru/NiFe-LDH@V_4C_3T_x$ locates between V foil and V_2O_5 and is higher than $NiFeAl-LDH@V_4C_3T_x$, certifying that the oxidation states of V in $Ru/NiFe-LDH@V_4C_3T_x$ is lower than V^{5+} and higher than $NiFeAl-LDH@V_4C_3T_x$ (Fig. 2d). The Ru K-edge XANES spectrum of $Ru/NiFe-LDH@V_4C_3T_x$ is shown in Fig. 2e. The near-edge absorption energy of $Ru/NiFe-LDH@V_4C_3T_x$ is between Ru foil and RuO_2, indicating that the oxidation state of Ru is between 0 and + 4 [17]. The aforementioned XAFS results are consistent with that of XPS, clearly confirming that the electron donated from conductive $V_4C_3T_x$ MXene and cation vacancies induce the strong electronic interaction between components and formation of electron-rich Ru, which would enhance the OER activity.

Furthermore, the extended X-ray absorption fine structure (EXAFS) spectroscopy was used to investigate the coordination environment. As shown in Fig. S19a, the peaks at 1.62 and 2.74 Å in the Ni K-edge Fourier-transform EXAFS (FT-EXAFS) of $Ru/NiFe-LDH@V_4C_3T_x$ are assigned to the Ni-O and Ni-M bonding (M=Ni or Fe) [50]. The EXAFS fitting results (Fig. S20 and Table S2) reveal that the coordination number (CN) of Ni-O and Ni-M shell in $Ru/NiFe-LDH@V_4C_3T_x$ is lower than that of NiFeAl-LDH and $NiFeAl-LDH@V_4C_3T_x$, demonstrating the presence of vacancies, especially metal vacancies. The Fe K-edge FT-EXAFS spectra of samples show the typical peaks of Fe-O and Fe-M (Fig. S19b) [51]. The CN of Fe-O in $Ru/NiFe-LDH@V_4C_3T_x$ is higher than other samples, suggesting the higher oxidation state of Fe (Fig. S21 and Table S2).

Besides, the peaks assigned to V-O, V-C and V-V coordination in V K-edge FT- EXAFS spectra can be identified (Fig. S19c). As shown in Fig. 2f, the main peak at 1.53 Å is attributed to the Ru-O bond [45,52] and a weak peak of Ru-Ru is located at 2.21 Å. The weak peak of Ru-Ru in

Ru/NiFe-LDH@$V_4C_3T_x$ indicates the existence of Ru cluster, which is consistent with the AC-HAADF-STEM image. The EXAFS fitting results indicate a CN of 4.3 for Ru-O, i.e. the Ru atom mainly coordinates with four oxygen to form Ru−O bonded to Ni or Fe (Fig. S22 and Table S2), thereby immobilizing Ru within the NiFe-LDH@$V_4C_3T_x$. In addition, the wavelet transform (WT) also exhibits the Ru-O coordination (Fig. 2g-i). The above-mentioned structure analysis confirms the stabilization of the Ru cluster by NiFe-LDH@$V_4C_3T_x$ and the strong metal-support interaction, which is closely relevant to the OER performance.

3.2. Electrocatalytic OER performance of Ru/NiFe-LDH@$V_4C_3T_x$

The OER performances of as-prepared samples were evaluated in 1 M KOH using a three-electrode. As shown in Fig. 3a, b, the linear sweep voltammetry (LSV) curves show that the Ru/NiFe-LDH@$V_4C_3T_x$ displays an overpotential of 231 mV at 10 mA cm^{-2}, lower than Ru/NiFeAl-LDH@$V_4C_3T_x$ (282 mV), Ru/NiFe-LDH (268 mV), NiFeAl-LDH@$V_4C_3T_x$ (248 mV), NiFeAl-LDH (334 mV), $V_4C_3T_x$ (467 mV) and RuO_2 (343 mV). Particularly, the Ru/NiFe-LDH@$V_4C_3T_x$ exhibits outstanding mass activity of 7741 mA mg_{Ru}^{-1} at overpotential of 270 mV. Such mass activity is several times larger than that of Ru/NiFeAl-LDH@$V_4C_3T_x$ (1509 mA mg_{Ru}^{-1}) and Ru/NiFe-LDH (2167 mA mg_{Ru}^{-1}) (Fig. S23a, b). The turnover frequency (TOF) is computed according to the loading amount of Ru, as shown in Fig. S23c, d. The TOF of Ru/NiFe-LDH@$V_4C_3T_x$ at overpotential of 270 mV is 10.3 s^{-1}, which is higher than Ru/NiFeAl-LDH@$V_4C_3T_x$ (2 s^{-1}) and Ru/NiFe-LDH (2.9 s^{-1}). Meanwhile, the TOF of Ru/NiFe-LDH@$V_4C_3T_x$ is still higher than that of control samples with the increase of overpotential. Furthermore, the Ru/NiFe-LDH@$V_4C_3T_x$ presents the smallest Tafe slope of 51 mV dec^{-1} (Fig. 3c), signifying the fast catalytic kinetics. The superior OER performance is obtained by optimizing the amount of MXene, Ru and molar ratio of Ni to Fe (Fig. S24 and S25). More importantly, the OER activity and Tafel slope surpass most of Ru-based and MXenes-based OER electrocatalysts (Fig. 3d, Table S3 and Table S4).

To evaluate the intrinsic activity of catalysts, the electrochemical surface area (ECSA) is quantified through double-layer capacitances

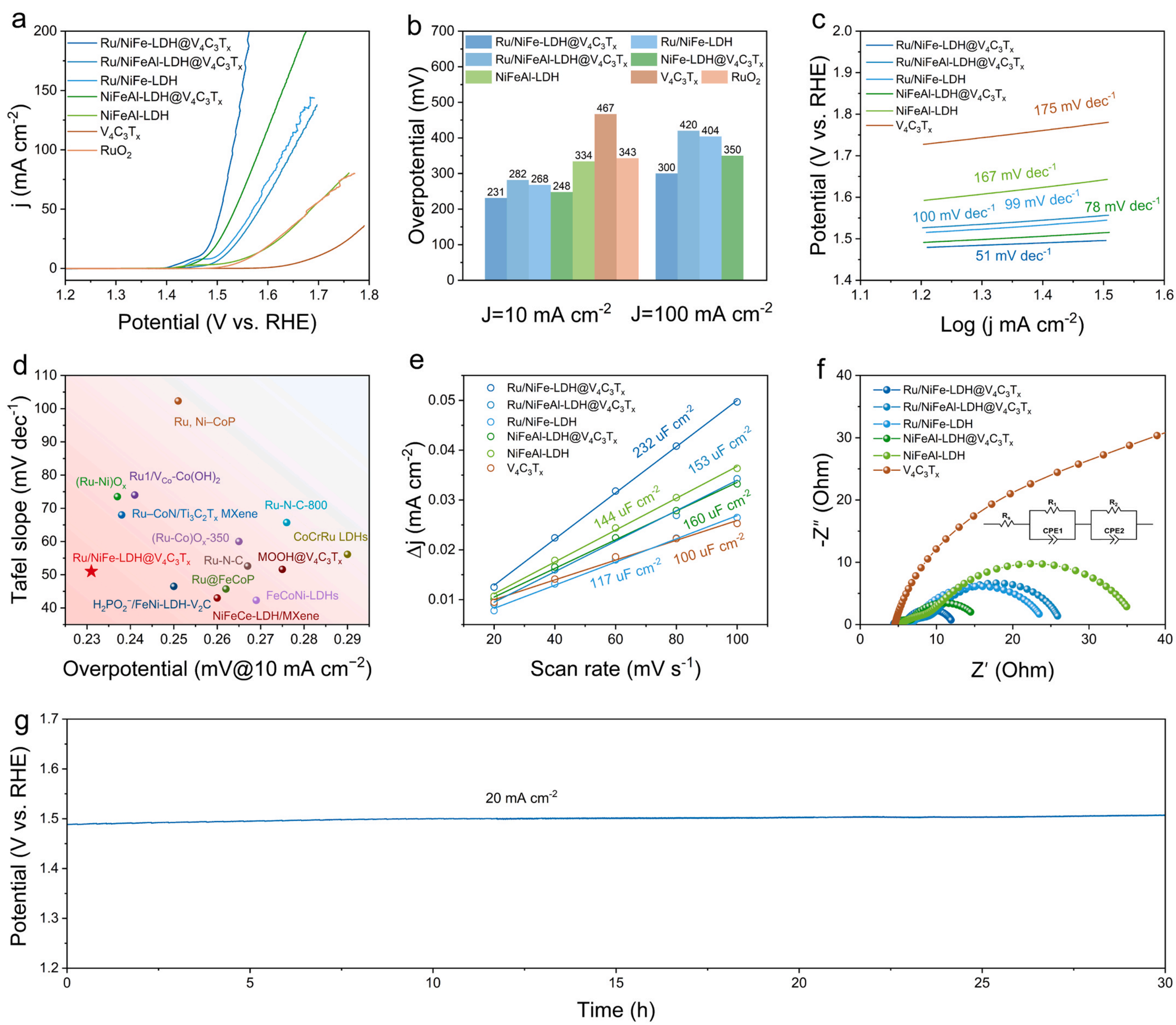

Fig. 3. OER performance of Ru/NiFe-LDH@$V_4C_3T_x$ and control samples. (a) LSV curves. (b) Comparison of overpotentials at 10 mA cm^{-2} and 100 mA cm^{-2}. (c) Tafel slope. (d) Comparison of overpotential at 10 mA cm^{-2} and Tafel slope of Ru/NiFe-LDH@$V_4C_3T_x$ with other reported state-of-the-art catalysts. (e) The plots of current density between anodic and cathodic vs scan rates. (f) EIS Nyquist plots at overpotential of 290 mV. (g) The chronopotentiometry curves at 20 mA cm^{-2}.

(Cdl). The Cdl is calculated from cyclic voltammetry (Fig. S26). As shown in Fig. 3e, the Ru/NiFe-LDH@$V_4C_3T_x$ possesses a higher Cdl value of 232 μF cm^{-2} than other samples, i.e. Ru/NiFe-LDH@$V_4C_3T_x$ has more active sites for improving its OER performance. Accordingly, the current density is normalized by the ECSA (Fig. S27). The current density of Ru/NiFe-LDH@$V_4C_3T_x$ is also significantly higher than other catalysts, indicating an improved intrinsic activity. Next, the electrochemical impedance spectroscopy (EIS) was conducted to investigate the charge transfer kinetics. The R_1 and R_2 in the equivalent circuit represent the resistance of electron-transfer across the liquid–solid interface and catalyst-glassy carbon electrode, respectively. Larger R_1 corresponds to the large charge transfer resistances (R_{ct}), and a slow charge transfer kinetics. The Ru/NiFe-LDH@$V_4C_3T_x$ shows a smaller R_{ct} compared to other samples, manifesting a much faster charge transfer kinetics (Fig. 3f). To evaluate the long-term stability, the continuous electrolysis was tested by chronopotentiometry at 20 mA cm^{-2}. The potential of Ru/NiFe-LDH@$V_4C_3T_x$ keeps at 1.507 V within 30 h (Fig. 3g), showing a good structural stability. Furthermore, the LSV curve reveals no obvious degradation of OER activity (Fig. S28). The higher oxidation states of Ru is often regarded to be responsible for the performance degradation. Thus, the Ru 3p XPS spectrum of Ru/NiFe-LDH@$V_4C_3T_x$ after OER was recorded to examine the change of Ru oxidation state. Similar position of Ru $3p_{3/2}$ peak for Ru/NiFe-LDH@$V_4C_3T_x$ catalysts before and after OER indicates that the oxidation state of Ru remains basically unchanged (Fig. S29a). Different from the observation for Ru, V ions are partially oxidized, as illustrated by the decreased peak intensities of V 2p located at the low binding energy (Fig. S30a). Similarly, Ni 2p spectrum in Fig. 4c shows an increase of Ni^{3+}, which is consistent with previous reports [42]. Comparatively, the valence state of Fe does not change obviously (Fig. S30b). XPS results reveal that, in OER process, V is more likely to lose electrons than Ru. Thus, the oxidation of V hinders the change of the valence state of Ru because of electron transfer between Ru clusters to NiFe-LDH@$V_4C_3T_x$. In addition, phase structure of catalyst Ru/NiFe-LDH@$V_4C_3T_x$ is well maintained, as evidenced by only presence of the diffraction peaks of LDHs (Fig. S29b). The TEM image of Ru/NiFe-LDH@$V_4C_3T_x$ after OER reveals the unchanged morphology (Fig. S31a). The Ru atom clusters and vacancies can be still observed in AC-HAADF-STEM image (Fig. S31b). The EDS mapping images display the uniform distribution of elements (Fig. S31c). Furthermore, the Ru content of Ru/Ni-Fe-LDH@$V_4C_3T_x$ after OER stability test is about 1.94 wt% (Table S5), very close to the initial value (Table S1). This result indicates that the Ru

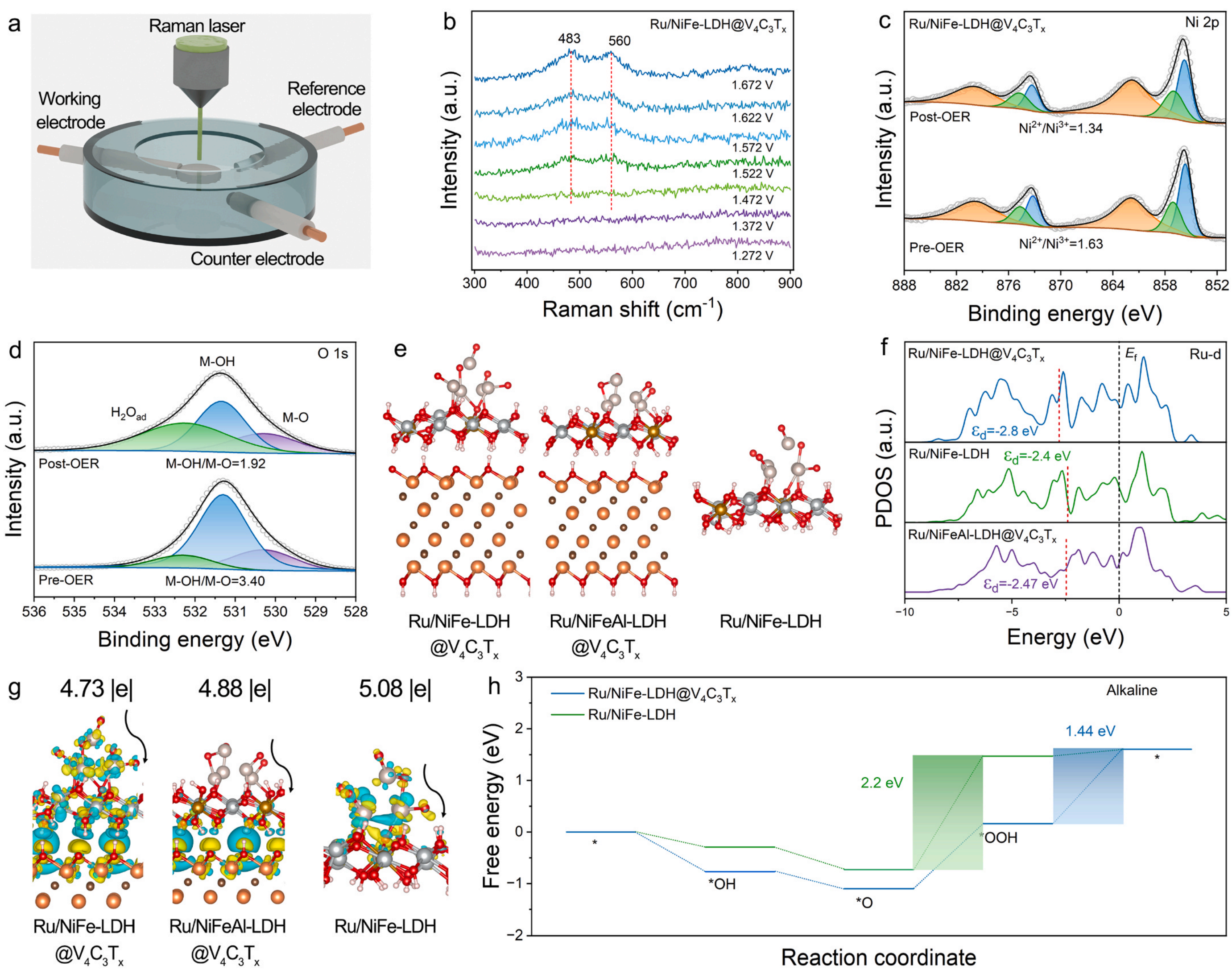

Fig. 4. In situ Raman, XPS spectra, and DFT calculations. (a) Schematic diagram of In situ Raman test. (b) In situ Raman spectra of Ru/NiFe-LDH@$V_4C_3T_x$ at different potentials. (c) Ni 2p and (d) O 1 s spectra of Ru/NiFe-LDH@$V_4C_3T_x$ before and after OER. (e) Optimized structures of Ru/NiFe-LDH@$V_4C_3T_x$, Ru/NiFeAl-LDH@$V_4C_3T_x$ and Ru/NiFe-LDH. (f) PDOS of Ru for Ru/NiFe-LDH@$V_4C_3T_x$, Ru/NiFeAl-LDH@$V_4C_3T_x$ and Ru/NiFe-LDH. (g) Electron density difference of Ru/NiFe-LDH@$V_4C_3T_x$, Ru/NiFeAl-LDH@$V_4C_3T_x$ and Ru/NiFe-LDH. (h) Free energy diagram of OER for Ru/NiFe-LDH@$V_4C_3T_x$ and Ru/NiFe-LDH.

in NiFe-LDH@$V_4C_3T_x$ remains stable in 1.0 M KOH electrolyte. In sum, thanks to the hierarchical structure and modulation of electron structure, the Ru/NiFe-LDH@$V_4C_3T_x$ shows superior catalytic activity and stability.

3.3. Structure evolution and theoretical calculations of Ru/NiFe-LDH@$V_4C_3T_x$

A detailed understanding of the structural and oxidation state evolution during the OER process is essential for understanding the catalytic mechanism of Ru/NiFe-LDH@$V_4C_3T_x$ with superior catalytic activity. In situ Raman spectra were carried out to investigate the structural evolution of Ru/NiFe-LDH@$V_4C_3T_x$ (Fig. 4a and Fig. S32). The Raman spectrum, recorded for the original Ru/NiFe-LDH@$V_4C_3T_x$ in the air, exhibits two signals at 478 and 556 cm^{-1} that are attributed to the Ni^{II}-O vibrations in NiFe-LDH (Fig. S33). While immersing the catalyst into a 1.0 M KOH electrolyte, both signals are absence at potential from 1.272 to 1.472 V due to the scattering effect of electrolyte (Fig. 4b). When potential was higher than 1.472 V, two peaks appeared at 483 and 560 cm^{-1}. Both peaks can be ascribed to the vibrations of Ni-O in NiOOH [42,53]. This observation indicates the formation of NiOOH phase. It is noteworthy that the formation of NiOOH phase occurs at higher potentials (1.522 V), which further demonstrates the stability of the structure. Besides, the Ni 2p and O 1 s XPS spectra at a higher potential were also investigated (Fig. 4c). The decreased ratio of Ni^{2+}/Ni^{3+} and M-OH/M-O further confirms the formation of more Ni^{3+}. Moreover, significantly increased peak intensity of oxygen species from the absorbed H_2O (Fig. 4d) indicates a remarkable hydrophilic characteristic.

The DFT calculations were carried out to insight the origins of enhanced OER performance. Based the in situ Raman analysis, the models were constructed by removing part of H atoms on the surface [53]. The Gibbs free energy of the OER intermediates for Ru/NiFe-LDH and Ru/NiFe-LDH@$V_4C_3T_x$ was calculated based on the optimized structure (Fig. S34, S35, S36). For the Fe and Ni sites of Ru/NiFe-LDH, the formation of O_2 (*OOH→1/2 O_2) is the rate-determine step (RDS) with a free energy barrier of 2.79 and 2.57 eV (Fig. S37a), while for the Ru site, the RDS of Ru/NiFe-LDH is the formation of *OOH with a low free energy barrier of 2.24 eV. Obviously, the evolution of O_2 is sluggish at Fe and Ni sites. Thus, the Ru site is considered as the active site. Comparatively, the free energy barrier of Ru/NiFe-LDH@$V_4C_3T_x$ for the RDS (*OOH→1/2 O_2) is larger than that of Ru/NiFe-LDH (Fig. S37b), contradictory with the experimental results. Therefore, the structure with Ru-O moiety is constructed to rationalize the DFT calculations (Fig. 4e). As shown in Fig. 4f, the partial density of states (PDOS) demonstrates the roles of $V_4C_3T_x$ MXene and cation vacancies on the enhanced OER performance. Specifically, the Ru d-band center of Ru/NiFe-LDH and Ru/NiFeAl-LDH@$V_4C_3T_x$ are − 2.4 and − 2.47 eV, respectively. The center of Ru/NiFe-LDH@$V_4C_3T_x$ obviously shifts to − 2.8 eV due to the co-existence of $V_4C_3T_x$ and vacancies, away from Fermi level, which is beneficial to modulate the absorption of intermediates. The charge redistribution visualized by electron density difference in Fig. 4g clarifies the origin of the shift for Ru d-band center. The Ru atoms in Ru/NiFe-LDH, Ru/NiFeAl-LDH@$V_4C_3T_x$ and Ru/NiFe-LDH@$V_4C_3T_x$ tend to donate electrons, Clearly, after introducing of $V_4C_3T_x$ into the composite, the denoted electrons of Ru/NiFeAl-LDH@$V_4C_3T_x$ is 4.88 |e|, smaller than 5.08 |e| for that of Ru/NiFe-LDH. For Ru/NiFe-LDH@$V_4C_3T_x$ with more vacancies, the denoted electrons further reduced to 4.73 |e|, which results in the formation of electron-rich Ru atoms [27]. The electron richness downshifts the d-band center of Ru atoms, thus optimizing the adsorption of intermediates. Consequently, the Ru/NiFe-LDH@$V_4C_3T_x$ shows a energy barrier of 1.44 eV for RDS, much lower than 2.2 eV for Ru/NiFe-LDH (Fig. 4h and Fig. S38). The change of RDS from the formation of *OOH to the conversion of *OOH→1/2 O_2 is attributed to the weak adsorption of *OOH, which corresponds to the downshift of the Ru d-band center [54,55].

4. Conclusion

In summary, we proposed a cooperative modulator to design noble-metal-based OER electrocatalysts. Ru clusters were successfully anchored onto a conductive NiFe-LDH@$V_4C_3T_x$ MXene substrate using a simple hydrothermal and etching process, wherein $V_4C_3T_x$ MXene functioned as a conductive substrate and an electron donor, modulating the electronic structures of Ru clusters as well as the cation vacancies. Our experimental analyses and DFT calculations demonstrated that the synergies of $V_4C_3T_x$ MXene and cationic vacancies induced electronic redistribution, leading to the formation of electron-rich Ru atoms and their lowered d-band center. Owing to the downshifting of the d-band center, the adsorption of *OOH weakened, and RDS switched to a low energy barrier, which significantly enhanced the OER activity of as-synthesized catalyst. In particular, Ru/NiFe-LDH@$V_4C_3T_x$ exhibited a low overpotential of 231 mV at 10 mA cm^{-2} in 1 M KOH and a high mass activity of 7741 mA mg_{Ru}^{-1} at an overpotential of 270 mV. Overall, our findings can be summarized as follows: (1) The introduction of cationic vacancies in NiFe-LDH facilitates the immobilization of Ru clusters. (2) The synergy between conductive $V_4C_3T_x$ MXene and cationic vacancies drives *d*-electron modulation around Ru clusters. (3) Electron-rich Ru clusters switch the RDS and reduce the free energy barrier, which boosts the OER activity. Thus, the findings of our study facilitate an improved understanding of the relationship between the catalytic activities and electronic structures of noble-metal-based catalysts and provide hints for the design of low-cost and efficient catalysts for practical applications.

CRediT authorship contribution statement

Yuan Zeyu: Formal analysis. **Li Yilin:** Visualization. **Li Junzhi:** Formal analysis, Investigation, Validation, Writing – original draft. **Wang Lili:** Formal analysis, Writing – review & editing. **Li Guangshe:** Funding acquisition, Resources, Writing – review & editing. **Li Liping:** Formal analysis, Funding acquisition, Resources, Supervision, Writing – review & editing. **Cui Jiawen:** Visualization. **Han Wei:** Resources, Supervision. **Li Dongdong:** Visualization. **Wang Mingrui:** Formal analysis. **Tang Haitong:** Data curation.

Declaration of Competing Interest

The authors declare that they have no known competing financial interests or personal relationships that could have appeared to influence the work reported in this paper.

Data Availability

Data will be made available on request.

Acknowledgements

The authors sincerely acknowledge financial support from the National Natural Science Foundation of China (NSFC Grant Nos. U20A20246, 22175070, 21871106 and 22293041) and Jilin Provincial Scientific and Technological Development Program (SKL202302018).

Appendix A. Supporting information

Supplementary data associated with this article can be found in the online version at doi.

References

[1] C. Lin, J.-L. Li, X. Li, S. Yang, W. Luo, Y. Zhang, S.-H. Kim, D.-H. Kim, S.S. Shinde, Y.-F. Li, Z.-P. Liu, Z. Jiang, J.-H. Lee, In-situ reconstructed Ru atom array on α-MnO_2 with enhanced performance for acidic water oxidation, Nat. Catal. 4 (2021) 1012–1023.

[2] S.P. Zeng, H. Shi, T.Y. Dai, Y. Liu, Z. Wen, G.F. Han, T.H. Wang, W. Zhang, X. Y. Lang, W.T. Zheng, Q. Jiang, Lamella-heterostructured nanoporous bimetallic iron-cobalt alloy/oxyhydroxide and cerium oxynitride electrodes as stable catalysts for oxygen evolution, Nat. Commun. 14 (2023) 1811.

[3] P. Liu, B. Chen, C. Liang, W. Yao, Y. Cui, S. Hu, P. Zou, H. Zhang, H.J. Fan, C. Yang, Tip-enhanced electric field: a new mechanism promoting mass transfer in oxygen evolution reactions, Adv. Mater. 33 (2021) 2007377.

[4] Z. Yin, M. Hu, J. Liu, H. Fu, Z. Wang, A. Tang, Tunable crystal structure of Cu–Zn–Sn–S nanocrystals for improving photocatalytic hydrogen evolution enabled by copper element regulation, J. Semicond. 43 (2022), 032701.

[5] C. Huang, Q. Zhou, D. Duan, L. Yu, W. Zhang, Z. Wang, J. Liu, B. Peng, P. An, J. Zhang, L. Li, J. Yu, Y. Yu, The rapid self-reconstruction of Fe-modified Ni hydroxysulfide for efficient and stable large-current-density water/seawater oxidation, Energy Environ. Sci. 15 (2022) 4647–4658.

[6] J. Li, K. Huang, Y. Huang, Y. Ye, M. Zioek, Z. Wang, S. Yue, M. Ma, J. Liu, K. Liu, S. Qu, Z. Zhao, Y. Zhang, Z. Wang, State-of-the-art advances in vacancy defect engineering of graphitic carbon nitride for solar water splitting, J. Semicond. 44 (2023), 081701.

[7] A. Song, Q.R. Huang, C.Y. Zhang, H.R. Tang, K. Zhang, C.C. Liu, F. Huang, Y. Cao, Highly efficient organic solar cells with improved stability enabled by ternary copolymers with antioxidant side chains, J. Semicond. 44 (2023), 082202.

[8] G. Mu, G. Wang, Q. Huang, Y. Miao, D. Wen, D. Lin, C. Xu, Y. Wan, F. Xie, W. Guo, R. Zou, A kinetic control strategy for one-pot synthesis of efficient bimetallic metal-organic framework/layered double hydroxide heterojunction oxygen evolution electrocatalysts, Adv. Funct. Mater. 33 (2023) 2211260.

[9] N. Zhang, Y. Hu, L. An, Q. Li, J. Yin, J. Li, R. Yang, M. Lu, S. Zhang, P. Xi, C. Yan, Surface activation and Ni-S stabilization in NiO/NiS_2 for efficient oxygen evolution, , Angew. Chem. Int. Ed. 61 (2022) (2022), 07217.

[10] T. Zhang, Y. Liu, L. Tong, J. Yu, S. Lin, Y. Li, H.J. Fan, Oxidation state engineering in octahedral Ni by anchored sulfate to boost intrinsic oxygen evolution activity, ACS Nano 17 (2023) 6770–6780.

[11] S. Liu, Y. Zhang, X. Mao, L. Li, Y. Zhang, L. Li, Y. Pan, X. Li, L. Wang, Q. Shao, Y. Xu, X. Huang, Ultrathin perovskite derived Ir-based nanosheets for high-performance electrocatalytic water splitting, Energy Environ. Sci. 15 (2022) 1672–1681.

[12] C. Feng, Z. Zhang, D. Wang, Y. Kong, J. Wei, R. Wang, P. Ma, H. Li, Z. Geng, M. Zuo, J. Bao, S. Zhou, J. Zeng, Tuning the electronic and steric interaction at the atomic interface for enhanced oxygen evolution, J. Am. Chem. Soc. 144 (2022) 9271–9279.

[13] C.-Z. Yuan, S. Wang, K. San Hui, K. Wang, J. Li, H. Gao, C. Zha, X. Zhang, D. A. Dinh, X.-L. Wu, Z. Tang, J. Wan, Z. Shao, K.N. Hui, In situ immobilizing atomically dispersed ru on oxygen-defective Co_3O_4 for efficient oxygen evolution, ACS Catal. 13 (2023) 2462–2471.

[14] J. Li, C. Hou, C. Chen, W. Ma, Q. Li, L. Hu, X. Lv, J. Dang, Collaborative interface optimization strategy guided ultrafine RuCo and MXene heterostructure electrocatalysts for efficient overall water splitting, ACS Nano 17 (2023) 10947–10957.

[15] Y. Zhu, J. Wang, T. Koketsu, M. Kroschel, J.M. Chen, S.Y. Hsu, G. Henkelman, Z. Hu, P. Strasser, J. Ma, Iridium single atoms incorporated in Co_3O_4 efficiently catalyze the oxygen evolution in acidic conditions, Nat. Commun. 13 (2022) 7754.

[16] L. Guo, J. Chi, J. Zhu, T. Cui, J. Lai, L. Wang, Dual-doping $NiMoO_4$ with multi-channel structure enable urea-assisted energy-saving H_2 production at large current density in alkaline seawater, , Appl. Catal. B Environ. 320 (2023), 121977.

[17] N. Yao, H. Jia, J. Zhu, Z. Shi, H. Cong, J. Ge, W. Luo, Atomically dispersed Ru oxide catalyst with lattice oxygen participation for efficient acidic water oxidation, Chem 9 (2023) 1–15.

[18] C. Rong, X. Shen, Y. Wang, L. Thomsen, T. Zhao, Y. Li, X. Lu, R. Amal, C. Zhao, Electronic structure engineering of single-atom Ru sites via Co-N_4 sites for bifunctional pH-universal water splitting, Adv. Mater. 34 (2022) 2110103.

[19] D. Wang, J. Xue, X. Ding, J. Wei, C. Feng, R. Wang, P. Ma, S. Wang, H. Cao, J. Wang, M. Zuo, S. Zhou, Z. Zhang, J. Zeng, J. Bao, Neighboring cationic vacancy assisted adsorption optimization on single-atom sites for improved oxygen evolution, ACS Catal. 12 (2022) 12458–12468.

[20] C. Dong, X. Zhang, J. Xu, R. Si, J. Sheng, J. Luo, S. Zhang, W. Dong, G. Li, W. Wang, F. Huang, Ruthenium-doped cobalt-chromium layered double hydroxides for enhancing oxygen evolution through regulating charge transfer, Small 16 (2020) 1905328.

[21] J. Chen, J. Huang, R. Wang, W. Feng, H. Wang, T. Luo, Y. Hu, C. Yuan, L. Feng, L. Cao, K. Kajiyoshi, C. He, Y. Liu, Z. Li, Y. Feng, Atomic ruthenium coordinated with chlorine and nitrogen as efficient and multifunctional electrocatalyst for overall water splitting and rechargeable zinc-air battery, Chem. Eng. J. 441 (2022), 136078.

[22] Y.M. Zhang, Z.Y. Yuan, L.J. Zhao, Y.L. Li, X.K. Qin, J.Z. Li, W. Han, L.L. Wang, Review of design routines of MXene materials for magnesium-ion energy storage device, Small 19 (2023) 2301815.

[23] J. Zhang, Y. Zhao, X. Guo, C. Chen, C.-L. Dong, R.-S. Liu, C.-P. Han, Y. Li, Y. Gogotsi, G. Wang, Single platinum atoms immobilized on an MXene as an efficient catalyst for the hydrogen evolution reaction, Nat. Catal. 1 (2018) 985–992.

[24] J. Chen, C. Chen, M. Qin, B. Li, B. Lin, Q. Mao, H. Yang, B. Liu, Y. Wang, Reversible hydrogen spillover in Ru-WO_{3-x} enhances hydrogen evolution activity in neutral pH water splitting, Nat. Commun. 13 (2022) 5382.

[25] W. Chen, B. Wu, Y. Wang, W. Zhou, Y. Li, T. Liu, C. Xie, L. Xu, S. Du, M. Song, D. Wang, Y. liu, Y. Li, J. Liu, Y. Zou, R. Chen, C. Chen, J. Zheng, Y. Li, J. Chen, S. Wang, Deciphering the alternating synergy between interlayer Pt single-atom and NiFe layered double hydroxide for overall water splitting, Energy Environ. Sci. 14 (2021) 6428–6440.

[26] J. Ge, D. Zhang, Y. Qin, T. Dou, M. Jiang, F. Zhang, X. Lei, Dual-metallic single Ru and Ni atoms decoration of MoS_2 for high-efficiency hydrogen production, , Appl. Catal. B Environ. 298 (2021), 120557.

[27] S. Zhou, H. Jang, Q. Qin, L. Hou, M. Kim, S. Liu, X. Liu, J. Cho, Boosting hydrogen evolution reaction by phase engineering and phosphorus doping on Ru/P-TiO_2, Angew. Chem. Int. Ed. 61 (2022) (2022), 12196.

[28] F. Li, G.F. Han, J.P. Jeon, T.J. Shin, Z. Fu, Y. Lu, J.B. Baek, Surface electronic modulation with hetero-single atoms to enhance oxygen evolution catalysis, ACS Nano 15 (2021) 11891–11897.

[29] Y. Pi, Z. Qiu, Y. Sun, H. Ishii, Y.F. Liao, X. Zhang, H.Y. Chen, H. Pang, Synergistic mechanism of sub-nanometric Ru clusters anchored on tungsten oxide nanowires for high-efficient bifunctional hydrogen electrocatalysis, Adv. Sci. 10 (2023) 2206096.

[30] N. Wen, Y. Xia, H. Wang, D. Zhang, H. Wang, X. Wang, X. Jiao, D. Chen, Large-scale synthesis of spinel $Ni_xMn_{3-x}O_4$ solid solution immobilized with iridium single atoms for efficient alkaline seawater electrolysis, Adv. Sci. 9 (2022) 2200529.

[31] G. Li, T. Sun, H.J. Niu, Y. Yan, T. Liu, S. Jiang, Q. Yang, W. Zhou, L. Guo, Triple interface optimization of Ru-based electrocatalyst with enhanced activity and stability for hydrogen evolution reaction, Adv. Funct. Mater. 33 (2023) 2212514.

[32] H. Yu, W. Wang, Q. Mao, K. Deng, Z. Wang, Y. Xu, X. Li, H. Wang, L. Wang, Pt single atom captured by oxygen vacancy-rich NiCo layered double hydroxides for coupling hydrogen evolution with selective oxidation of glycerol to formate, , Appl. Catal. B Environ. 330 (2023), 122617.

[33] Q. Lin, L. Wang, Layered double hydroxides as electrode materials for flexible energy storage devices, J. Semicond. 44 (2023), 041601.

[34] J. Jin, X. Han, Y. Fang, Z. Zhang, Y. Li, T. Zhang, A. Han, J. Liu, Microenvironment engineering of Ru single-atom catalysts by regulating the cation vacancies in NiFe-layered double hydroxides, Adv. Funct. Mater. 32 (2022) 2109218.

[35] H. Zhang, L. Wu, R. Feng, S. Wang, C.-S. Hsu, Y. Ni, A. Ahmad, C. Zhang, H. Wu, H.-M. Chen, W. Zhang, Y. Li, P. Liu, F. Song, Oxygen vacancies unfold the catalytic potential of NiFe-layered double hydroxides by promoting their electronic transport for oxygen evolution reaction, ACS Catal. 13 (2023) 6000–6012.

[36] Y. Liu, X. Liu, A.R. Jadhav, T. Yang, Y. Hwang, H. Wang, L. Wang, Y. Luo, A. Kumar, J. Lee, H.T.D. Bui, M. Kim, H. Lee, Unraveling the function of metal-amorphous support interactions in single-atom electrocatalytic hydrogen, Evol., Angew. Chem. Int. Ed. 61 (2022) 202114160.

[37] Z. Yuan, Q. Lin, Y. Li, W. Han, L. Wang, Effects of multiple ion reactions based on a $CoSe_2$/MXene cathode in aluminum-ion batteries, Adv. Mater. 35 (2023) 2211527.

[38] L. Zhao, H. Xu, L.C. Liu, Y.Q. Zheng, W. Han, L.L. Wang, MXene-induced flexible, water-retention, semi-interpenetrating network hydrogel for high-performance, ultra-stable strain sensors, Adv. Sci. 10 (2023) 2303922.

[39] L. Wang, Y. Han, H. Wang, Y. Han, J. Liu, G. Lu, H. Yu, A. MXene-functionalized, paper-based electrochemical immunosensor for label-free detection of cardiac troponin I, J. Semicond. 42 (2021), 092601.

[40] X. Peng, S. Zhao, Y. Mi, L. Han, X. Liu, D. Qi, J. Sun, Y. Liu, H. Bao, L. Zhuo, H. L. Xin, J. Luo, X. Sun, Trifunctional single-atomic Ru sites enable efficient overall water splitting and oxygen reduction in acidic media, Small 16 (2020) 2002888.

[41] X. Chen, M. Yu, Z. Yan, W. Guo, G. Fan, Y. Ni, J. Liu, W. Zhang, W. Xie, F. Cheng, J. Chen, Boosting electrocatalytic oxygen evolution by cation defect modulation via electrochemical etching, CCS Chem. 3 (2021) 675–685.

[42] H. Lei, L. Ma, Q. Wan, S. Tan, B. Yang, Z. Wang, W. Mai, H.J. Fan, Promoting surface reconstruction of NiFe layered double hydroxide for enhanced oxygen evolution, Adv. Energy Mater. 12 (2022) 2202522.

[43] H. You, D. Wu, D. Si, M. Cao, F. Sun, H. Zhang, H. Wang, T.F. Liu, R. Cao, Monolayer NiIr-layered double hydroxide as a long-lived efficient oxygen evolution catalyst for seawater splitting, J. Am. Chem. Soc. 144 (2022) 9254–9263.

[44] Y. Zhu, A. Sikandaier, Y. Zhang, X. Wang, B. Du, J. Xue, Y. Sun, P. Lu, D. Yang, FeO@FeP heterostructure: surface phosphorization toward efficient photocatalytic Fenton-like norfloxacin removal, Environ. Funct. Mater. 1 (2022) 230–238.

[45] Y. Yang, Q.-N. Yang, Y.-B. Yang, P.-F. Guo, W.-X. Feng, Y. Jia, K. Wang, W.-T. Wang, Z.-H. He, Z.-T. Liu, Enhancing water oxidation of Ru single atoms via oxygen-coordination bonding with NiFe layered double hydroxide, ACS Catal. 13 (2023) 2771–2779.

[46] Z. Fang, Y. Liu, C.Y. Song, P. Tao, W. Shang, T. Deng, X.Q. Zeng, J.B. Wu, In-situ monitoring of dynamic behavior of catalyst materials and reaction intermediates in semiconductor catalytic processes, J. Semicond. 43 (2022), 041104.

[47] J. Zhou, S. Lin, Y. Huang, P. Tong, B. Zhao, X. Zhu, Y. Sun, Synthesis and lithium ion storage performance of two-dimensional V_4C_3 MXene, Chem. Eng. J. 373 (2019) 203–212.

[48] T. Luo, J. Huang, Y. Hu, C. Yuan, J. Chen, L. Cao, K. Kajiyoshi, Y. Liu, Y. Zhao, Z. Li, Y. Feng, Fullerene lattice-confined Ru nanoparticles and single atoms synergistically boost electrocatalytic hydrogen evolution reaction, Adv. Funct. Mater. 33 (2023) 2213058.

[49] Q. Liang, Q. Li, L. Xie, H. Zeng, S. Zhou, Y. Huang, M. Yan, X. Zhang, T. Liu, J. Zeng, K. Liang, O. Terasaki, D. Zhao, L. Jiang, B. Kong, Superassembly of surface-enriched Ru nanoclusters from trapping-bonding strategy for efficient hydrogen evolution, ACS Nano 16 (2022) 7993–8004.

[50] X. Chen, J. Wan, J. Wang, Q. Zhang, L. Gu, L. Zheng, N. Wang, R. Yu, Atomically dispersed ruthenium on nickel hydroxide ultrathin nanoribbons for highly efficient hydrogen evolution reaction in alkaline media, Adv. Mater. 33 (2021) 2104764.
[51] H. Yang, L. Gong, H. Wang, C. Dong, J. Wang, K. Qi, H. Liu, X. Guo, B.Y. Xia, Preparation of nickel-iron hydroxides by microorganism corrosion for efficient oxygen evolution, Nat. Commun. 11 (2020) 5075.
[52] Y. Wang, S. Wang, Z.L. Ma, L.T. Yan, X.B. Zhao, Y.Y. Xue, J.M. Huo, X. Yuan, S. N. Li, Q.G. Zhai, Competitive coordination-oriented monodispersed ruthenium sites in conductive MOF/LDH heteronanotree catalysts for efficient overall water splitting in alkaline media, Adv. Mater. 34 (2022) 2107488.
[53] P.L. Zhao, L. Li, G.X.J. Chen, X.X. Guan, Y. Zhang, W.W. Meng, L.G. Zhao, K.X. Li, R.H. Jiang, S.F. Jia, H. Zheng, J.B. Wang, Structural evolution of low-dimensional metal oxide semiconductors under external stress, J. Semicond. 43 (2022), 041105.
[54] X. Zheng, Y. Cao, Z. Wu, W. Ding, T. Xue, J. Wang, Z. Chen, X. Han, Y. Deng, W. Hu, Rational design and spontaneous sulfurization of NiCo-(oxy) hydroxysulfides nanosheets with modulated local electronic configuration for enhancing oxygen electrocatalysis, Adv. Energy Mater. 12 (2022) 2103275.
[55] L. Li, G. Zhang, J. Xu, H. He, B. Wang, Z. Yang, S. Yang, Optimizing the electronic structure of ruthenium oxide by neodymium doping for enhanced acidic oxygen evolution catalysis, Adv. Funct. Mater. 33 (2023) 2213304.